WILEY | Hindawi

Research Article

Exploration of Bifunctionality in Mn, Co Codoped CuO Nanoflakes for Overall Water Splitting

B. Jansi Rani [ID],[1] **P. Mohana** [ID],[1] **S. Swathi** [ID],[1] **R. Yuvakkumar** [ID],[1] **G. Ravi** [ID],[1,2] **M. Thambidurai** [ID],[3] **Hung D. Nguyen** [ID],[3] and **Dhayalan Velauthapillai** [ID][4]

[1]*Department of Physics, Alagappa University, Karaikudi, 630 003 Tamil Nadu, India*
[2]*Department of Physics, Chandigarh University, Mohali, 140 413 Punjab, India*
[3]*School of Electrical and Electronic Engineering, Nanyang Technological University, 50 Nanyang Avenue, Singapore 639798*
[4]*Faculty of Engineering and Science, Western Norway University of Applied Sciences, Bergen 5063, Norway*

Correspondence should be addressed to R. Yuvakkumar; yuvakkumarr@alagappauniversity.ac.in
and Dhayalan Velauthapillai; dhayalan.velauthapillai@hvl.no

Herein, bimetal (Mn, Co) codoping on a CuO host is aimed at enhancing oxygen evolution reaction (OER) and hydrogen evolution reaction (HER) activity. Codoping of Mn and Co on CuO to enhance bifunctional action in electrochemical water splitting has not yet been investigated to the best of our knowledge. Literatures are focused on unary Mn-doped CuO or Co-doped CuO nanostructures. Mn, Co codoped CuO through an easy chemical coprecipitation method has been successfully attempted and is more beneficial which is the novelty of the present work. Defect-enriched ample active sites (Mn^{2+}/Mn^{3+} and Co^{2+}/Co^{3+}) along with Cu^{2+} in the host CuO achieved high current density ($100\,mA/cm^2$) in OER and HER with low overpotential such as 468 mV and 271 mV, respectively. Faster charge transfer and diffusion ability was stimulated by the bimetal codoping CuO. Reasonable Tafel plot values (OER: 199 mV/dec, and HER: 21 mV/dec) with improved water-splitting reaction kinetics were achieved for the Mn, Co codoped CuO nanoflakes. The double-layer capacitance (C_{dl}) value of $27.5\,mF/cm^2$ for Mn, Co codoped CuO nanoflakes was achieved. Similarly, the increasing order of an electrochemically active surface area (EASA) was exhibited by the consequent addition of bimetal doping on CuO, denoted as Mn, Co/CuO > Co/CuO > Mn/CuO > CuO. The evidence shows that the codoping strategy could facilitate rapid reaction kinetics to develop overall water splitting. The charge transfer resistances (R_{ct}) of $3.6\,\Omega$ and $1.2\,\Omega$ for the Mn, Co codoped CuO nanostructure corresponding to the OER and HER, respectively, were reported. The long-term stability over 16 h with negligible loss was reported for both the OER and the HER performance. Thus, this work contributes to better insight and analysis of the successful codoping of bimetal elements in earth-abundant electrocatalysts to enhance and make practical the electrocatalytic water-splitting activity.

1. Introduction

The ever-increasing global energy demand caused by the expenditure of traditional fossil fuels has induced the alternative solution for clean and sustainable energy production [1]. Recently, hydrogen was considered a clean renewable energy carrier due to its carbon-free emission, high gravimetric energy density, and environmental benignity [2]. Electrocatalytic water splitting is a potential approach to produce hydrogen, which can satisfy upcoming energy requirements without greenhouse gas emissions [3, 4]. To the core, water splitting has 2 half-reactions, namely, hydrogen evolution reaction (HER) and oxygen evolution reaction (OER) [5]. HER requires 2 electrons ($2H^+ + 2e^- \rightarrow H_2$) in the cathode side and OER requires four electrons ($4OH^- \rightarrow O_2 + 2H_2O$) in the anode side [6]. However, OER is notably a sluggish reaction compared to HER, which leads the overall water splitting to be associated with a high driving force [7]. So far, the noble metals like Pt (for HER) and RuO_2/IrO_2 (for OER) are reported as benchmark commercial electrocatalysts for water splitting [8–11]. The high cost and less accessibility of the above-mentioned potential catalysts

hinder the economic progress commercially, and the requirement of the low-cost transition metal-based electrocatalysts for energy production is raised as a major problem. In this time, there is need to regenerate the effective electrocatalysts by using naturally rich elements as the suitable ideal solution for the imminent energy-related issues [12]. There are many strategies that manipulate the electrochemical activity to improve bifunctionality of the working electrode. Among them, doping is one of the tantalizing yet conventional approaches to influence electrochemical properties of electrocatalysts. Specifically, transition metal-based elements get more attention because of flexibility, conductivity, multiple valence states, and natural abundance [13]. Since efficient electrocatalysts with a low driving force (overpotential) and superior chemical and thermal stability are necessary for the continuous research in this field, Lv et al. explored the synthesis of a nanostructured substrate-integrated growth $CuO@Cu_3P$ on Cu foam for overall water splitting with low overpotentials (144 mV for HER and 267 mV for OER at 10 mA/cm^2) [14]. Yin et al. succeeded in the in situ growth of CuO@CoZn-LDH nanoarrays for proficient overall water splitting [15]. Maiti and Srivastava reported Ru-doped CuO/MoS_2 nanostructures for an efficient HER (~198 mV) and OER (201 mV) to attain 10 mA/cm^2 [16]. Thus, CuO-based electrocatalysts with the implementation of some attractive approaches like doping, morphology engineering, composite/heterojunction formations, and layered deposition are gaining more attention due to their improved electrocatalytic activity [17–21], since it is one of the cheapest elements on earth. In the doping strategy, codoping is an efficient and promising tactic to encourage the electrocatalytic activity of the material [22, 23].

Markedly, Mn and Co are the well-known electrocatalysts for both OER and HER because of conductivity, multiple valence states, and inherent catalytic activity [24–28]. Owing to the consideration of cost-effectiveness and earthly abundance, CuO was chosen as the electrocatalyst. Besides, Mn and Co are utilized as a dopant, and controlling the active sites via morphology is an additional strategy implemented in this work to enhance the conductivity. The sharp-edge nanoneedles, nanoflakes, nanoplates, and nanorods are the fascinating morphology to create abundant polarized zones for easy electron transfer in electrocatalytic reactions [29, 30]. Therefore, no reports are available on codoping of Mn and Co on CuO with a unique nanoflake morphology which stimulates to perceive the structural, morphological, and electrochemical nature of a produced sample for electrocatalytic water splitting. The modern researches seek a low-cost alternative to produce clean energy for advanced hydrogen fuel economy. The present report examines the codoping strategy on CuO nanoflakes to improve the bifunctional activity for water splitting; it achieved a low driving potential for OER and HER at a high current density. It is an insightful outcome to the high performance of large-scale electrolyzers in the near future.

In this work, the Mn, Co codoped CuO nanoflakes were synthesized using a facile coprecipitation method followed by thermal annealing as an excellent bifunctional catalyst for electrocatalytic water splitting. The successful codoping

and the presence of Mn and Co on the CuO host have been confirmed via X-ray diffraction (XRD) and energy-dispersive spectra (EDS), respectively. More valence state numbers provoked bifunctionality which is reported by the lower overpotential requirement for OER (468 mV) and HER (271 mV) at a high density of 100 mA/cm^2. High conductivity, rapid reaction kinetics, and long-term stability over 20 h of Mn, Co codoped CuO nanoflakes are reported for the real-time electrocatalytic water-splitting application.

2. Methods

2.1. Materials Used. Copper chloride dihydrate ($CuCl_2 \cdot 2H_2O$), manganese chloride tetrahydrate ($MnCl_2 \cdot 4H_2O$), cobalt chloride hexahydrate ($CoCl_2 \cdot 6H_2O$), sodium hydroxide (NaOH), ethanol (C_2H_5OH), and deionized (DI) water were purchased from Sigma-Aldrich. Ni foam was procured from the Zopin Group. Pt, graphite rod, and Ag/AgCl were also procured.

2.2. CuO, Mn-doped, Co-doped, and Mn, Co codoped CuO Nanoflake Preparation. Typically, 0.5 M of copper chloride was dissolved into 50 ml deionized water and kept in the magnetic stirrer for 15 min. Consequently, 5 M of the NaOH solution was prepared and named as solution B and dropwise added into solution A. Then, the mixed solution was adjusted at pH 11 by adding NaOH. Then, the mixed solution A was left free for 12 h to form precipitate. The substance gets filtered by using deionized water, methanol, and ethanol twice and is further dried at 80°C for 12 h. The final sample was annealed at 400°C, and the powder was considered as pure CuO nanoflakes. Then, Mn-CuO and Co-CuO nanoflakes were produced like that of pure CuO, nevertheless with the molar amount of 0.01 M of $MnCl_2 \cdot 4H_2O$ and $CoCl_2 \cdot 6H_2O$, separately added in the 0.49 M of the $CuCl_2 \cdot 2H_2O$ (50 ml) solution. Finally, Mn, Co codoped CuO nanoflakes were produced by simultaneously adding 0.01 M of $MnCl_2 \cdot 4H_2O$ and $CoCl_2 \cdot 6H_2O$ in 0.48 M of the $CuCl_2 \cdot 2H_2O$ (50 ml) solution. The obtained four powders were denoted as pure CuO, Mn-CuO, Co-CuO, and Mn, Co-CuO, respectively, as depicted in Figure 1 [31, 32]. The physical characterizations of the synthesized nanoflakes were done by using the same instruments, and measuring conditions are reported in detailed previous works [33, 34].

2.3. Electrode Preparation. The electrochemical studies of synthesized nanoflakes were done in a 3-electrode half-cell setup, where Pt and a graphite rod were employed as the counter for OER and HER, Ag/AgCl was employed as a reference, and the active materials (CuO, Mn-CuO, Co-CuO, and Mn, Co-CuO) on the Ni foam were used as working electrodes. The working electrode fabrication was the same as that of a previous work [35]. The active material loaded on the Ni foam was ~2.5 mg/cm^2, and the geometrical dimension of the working electrode area was 1 cm × 1 cm.

3. Results and Discussion

3.1. Structural Characterizations of Pure, Mn-doped, Co-doped, and Mn, Co codoped CuO Nanoflakes. The coprecipitation technique was employed for the successful production
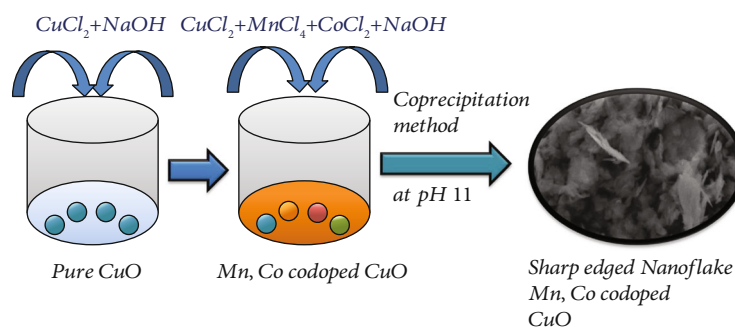
FIGURE 1: Production methodology of Mn, Co codoped CuO.

of pure, Mn-doped, Co-doped, and Mn, Co codoped CuO nanoflakes as competent bifunctional electrocatalysts. The well-off doping on the monoclinic crystal structure of CuO was confirmed via XRD spectra as shown in Figure 2(a). Well-defined diffraction peaks observed for the crystal planes such as (110), (-111), (111), (202), (020), (-202), (-113), (-311), (220), (311), and (-222) are matched very well with the JCPDS #48-1548 of the monoclinic CuO [36, 37]. No other anonymous peaks are observed for the synthesized pure and doped samples, which revealed the optimal incorporation of Mn and Co in the Cu position of CuO. The monoclinic crystal structure of the host frame is illustrated in Figure 2(b). Besides, the codoping certainly affected the crystal nature, which caused the formation of ample defects. The calculated crystallite sizes (using the Debye-Scherer formula [38]) of CuO, Mn-doped, Co-doped, and Mn, Co codoped CuO are around 32 ± 3 nm (32, 31, 35, and 29 nm, respectively).

Raman spectra of produced products shown in Figure 2(c) represent phonon vibration modes around ~299 and ~634 cm^{-1}, with an inhomogeneous hump throughout the range (caused by surface defects) [39]. The Raman bands ~299 and ~634 cm^{-1} explored the A_g and B_g modes of monoclinic CuO, respectively [40]. The shifts in A_g mode corresponding to the Mn-doped, Co-doped and Mn, Co codoped CuO further confirm the doping, where the A_g mode is more sensitive to the dopants [41]. The surface intrinsic emission regions and oxygen vacancies/defects were examined via photoluminescence (PL) spectra (Figure 2(d)). The PL spectra were obtained at 320 nm excitation. The observed peaks at 361, 377, 411, 495, 506, and 520 nm were observed in photoluminescence spectra of Mn, Co codoped CuO nanoflakes as shown in Figure 2(d). The peak at 361 and 377 nm was attributed to the near band edge (NBE) emission of CuO [42]. 411 and 495 nm were obviously ascribed to the blue shift performance where the violet-to-blue emission gets shifted which corresponds to the transition of oxygen vacancies and interstitial oxygen defects present in the sample. The recombination of holes and electrons occupies the ionized oxygen vacancies in the green emission regions which are allocated to the wavelength at 506 and 520 nm [43]. The PL emission peaks with different intensities were aroused due to the surface structural behavior of the prepared samples.

An FTIR study of pure and doped CuO nanoflakes is demonstrated in Figure 2(e). The stretching and bending vibration modes of the metal-oxygen bond with functional groups adsorbed at the surface of the material have been characterized at 4000-400 cm^{-1}. The vibration bands observed at 607 and 874 cm^{-1} in the fingerprint region of FTIR explored the stretching of Cu and O [44]. The other vibration bands observed at 1098, 1458, 1640, 2358, 2923, and 3466 cm^{-1} were attributed to C-O stretching, CH$_2$, OH bending, CO$_2$, C-H, and OH stretching of the adsorbed radicals, respectively [45]. Moreover, the steep OH stretching band observed for Mn, Co codoped CuO suggests more hydrophilic groups present at the surface [46]. Notably, the XRD pattern (Figure 2(a)) shows that the high intensity of undoped CuO authenticates the phase confirmation and purity of CuO formation, and the peak shift appeared in the Mn, Co codoped CuO at lower angles due to the constant lattice variations. The bimetal Mn and Co has a nearly similar range of ionic radius ranges (0.06 to 0.08 A^0) which is incorporated into the CuO lattice which does not affect the monoclinic phase; nevertheless, it slightly gets shifted due to the intercalation which occurred in the lattice cell arrangements which make considerable change in the intensification of the crystal size which is noticed in Figure 2(f). The peak shift at the lattice planes of (-111) and (111) slightly corresponds with the 2θ values of 35.4° for pure CuO shifted into 35.2° for the doped CuO (Mn and Co) and 38.5° to 38.6° for pure and doped CuO, respectively [47].

Scanning electron microscope (SEM) images of pure and doped CuO (Figure 3) revealed the nanostructured morphology of all four products. Figure 3(a) shows the aggregated nanoflake morphology of bare CuO, which acted as a frame for the sharp-edge nanoflake formation of the other doped samples. Figures 3(b) and 3(c) represent the same kind of nanoflake morphology of Mn- and Co-doped CuO with less aggregation. Figure 3(d) confirms the sharp-edge-rich triangular nanoflakes of Mn, Co codoped CuO [48]. The particle size of all four samples also could be estimated from Figures 3(a)–3(d), which reveal the nanoflake length to be around 110 ± 15, 100 ± 20, 95 ± 15, and 85 ± 10 nm, respectively, for CuO, Mn-CuO, Co-CuO, and Mn, Co codoped CuO nanoflakes. Hence, SEM studies of Mn, Co codoped CuO nanostructures reveal that the unique sharp-edged nanoflake-like structure covered with a rough surface exhibited a tiny particle size which indicates that the capability of the porous nature consists of numerous active sites on the electrode surface for electron hole transportation, and sharp edges were helpful for the bubble formation which is
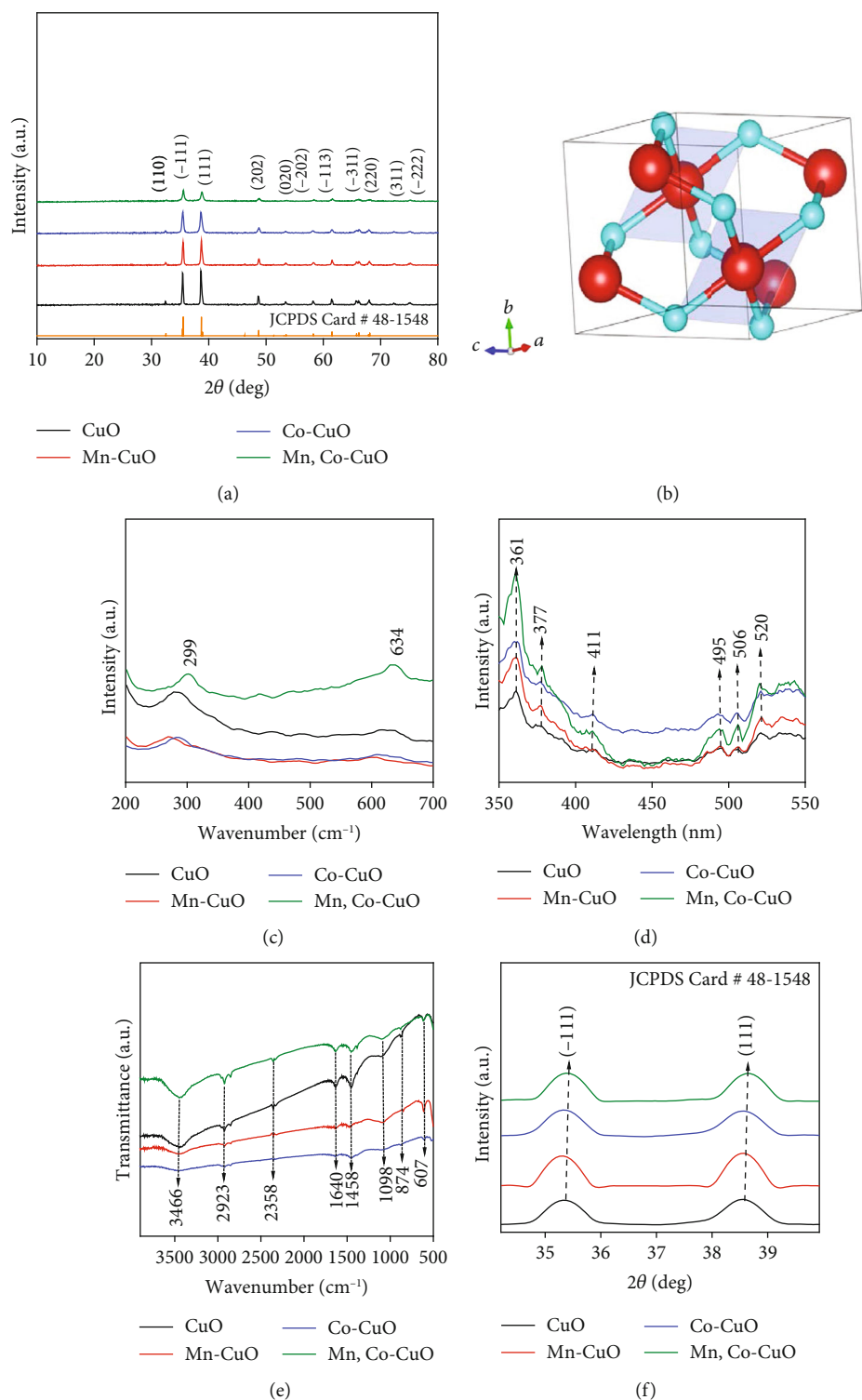
FIGURE 2: Structural characterizations of Mn, Co, and codoped CuO nanoflakes: (a) X-ray diffraction (XRD); (b) crystal structure; (c) Raman spectra; (d) photoluminescence; (e) Fourier transform infrared (FTIR); (f) peak shift pattern of Mn, Co codoped CuO.

the strong beneficial behavior for oxygen and hydrogen evolution in an effective way. Hence, the nanoflake morphology structure of Mn, Co codoped CuO affirms a strong electrolyte ion transport and performs as a more superficial electroactive species for the electrocatalytic performances [49, 50]. In addition, it provided a high electrochemically active surface area (discussed in the latter part) which undeniably supports the overall reaction kinetics of water splitting. Moreover, Mn and Co codoping on the CuO host is further evidently confirmed from the energy-dispersive spectra (EDS) shown in Figure 3(e), and the uniform allotments of Mn, Co, Cu, and O were demonstrated from EDS mapping

(a)

(b)

(c)

(d)

Element	Line type	Apparent concentration	K Ratio	Wt%	Wt% Sigma	Atomic%
O	K series	23.49	0.07906	24.14	0.71	55.68
Mn	K series	0.52	0.00520	1.33	0.94	0.89
Co	K series	1.20	0.01205	3.13	2.00	1.96
Cu	Lseries	22.90	0.22895	71.40	1.69	41.46
Total:				100.00		100.00

(e)

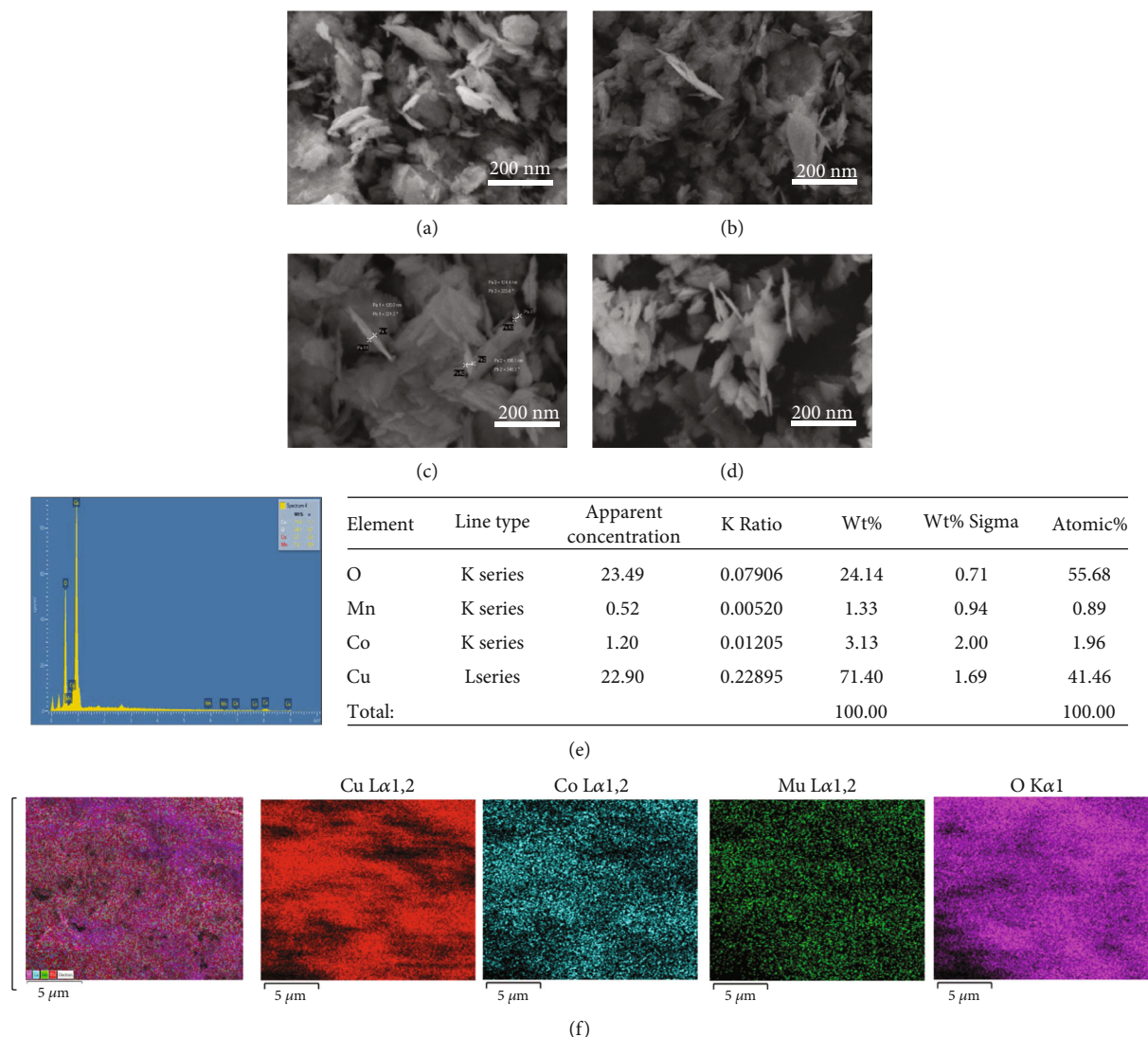Cu Lα1,2   Co Lα1,2   Mu Lα1,2   O Kα1

(f)

FIGURE 3: Morphological and elemental analyses: (a–d) scanning electron microscopy (SEM) of pure, Mn-doped, Co-doped, and Mn, Co codoped CuO, respectively; (e, f) energy-dispersive spectrum (EDS) results and mapping of Mn, Co codoped CuO nanoflakes.

(Figure 3(f)) [51]. Moreover, the significant insight of the morphology information was explored via transmission electron microscopy (TEM) (Figures 4(a)–4(f)). Figures 4(a)–4(c) explore TEM images of the prepared Mn, Co codoped CuO nanoflakes at different magnifications. The observed results clearly resemble nanoflake morphology which is consistent with the primary SEM images of the Mn, Co codoped CuO electrode. Figures 4(d) and 4(e) representing high-resolution transmission electron microscopy (HR-TEM) studies of the electrode reveal the clear lattice fringes with polycrystalline structure which is well in accordance with the XRD analysis. Also, the d-spacing values were calculated from the selected area electron diffraction (SAED) pattern which exposed few bright diffraction spots, confirmed the crystalline nature of the sample, and were well consistent with the observed XRD lattice planes (110), (-111), (111), (202), (020), (-113), (220), and (-222) which is shown in Figure 4(f). The interlayer structure of the achieved sharp-edge morphology

will increase the rate of electron transportation to enhance the electrocatalytic activities [52, 53].

The composition, electronic structures, and oxidation states of prepared Mn, Co codoped CuO nanoflakes were explored by employing X-ray photoelectron spectroscopy (XPS) as presented in Figures 5(a)–5(e). Figure 5(a) explores the overall survey spectra of the Mn, Co codoped CuO which confirms the Mn, Co, Cu, and O elements. The Mn2p spectrum is revealed in Figure 5(b) with peaks at 641.2 eV and 648.38 eV for the $Mn2p_{3/2}$ and $Mn2p_{1/2}$, respectively. It denotes Mn^{2+} oxidation states and a shakeup peak which occurred at 648.38 eV, which are well related to the previous literature. The deconvoluted Co2p spectra were observed in the peak values at 782.59 eV corresponding to the binding energy state of $Co2p_{3/2}$ (Figure 5(c)), yet low intense peaks have occurred due to the low content of cobalt, and it is also the evidence for the existence of $Co^{2+/3+}$ ions. The high intense Cu2p core level spectra split into 2 peaks
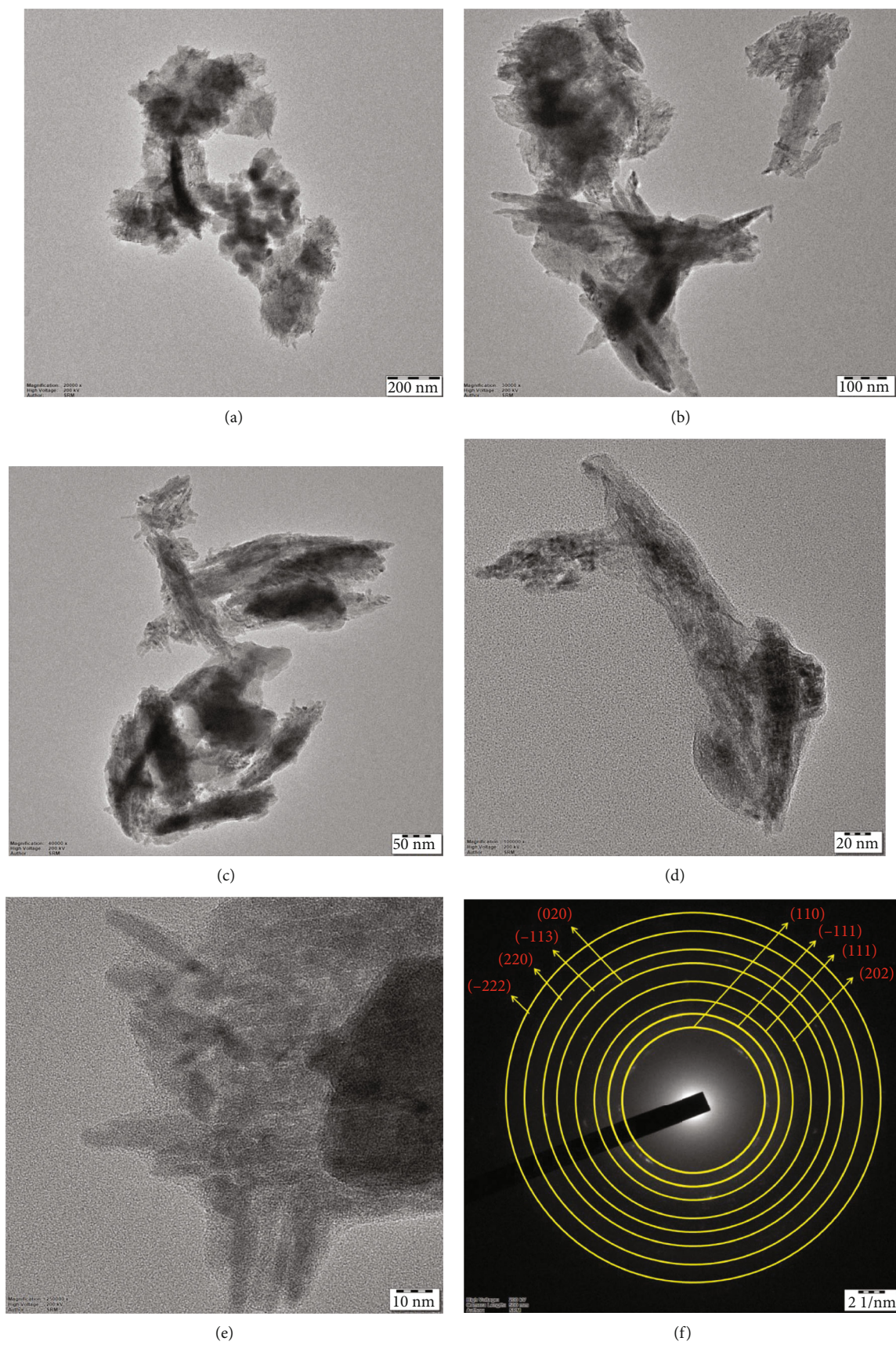
(a)

(b)

(c)

(d)

(e)

(f)

FIGURE 4: (a–c) TEM analysis; (d, e) HR-TEM; (f) SAED pattern of Mn, Co codoped CuO nanoflakes.
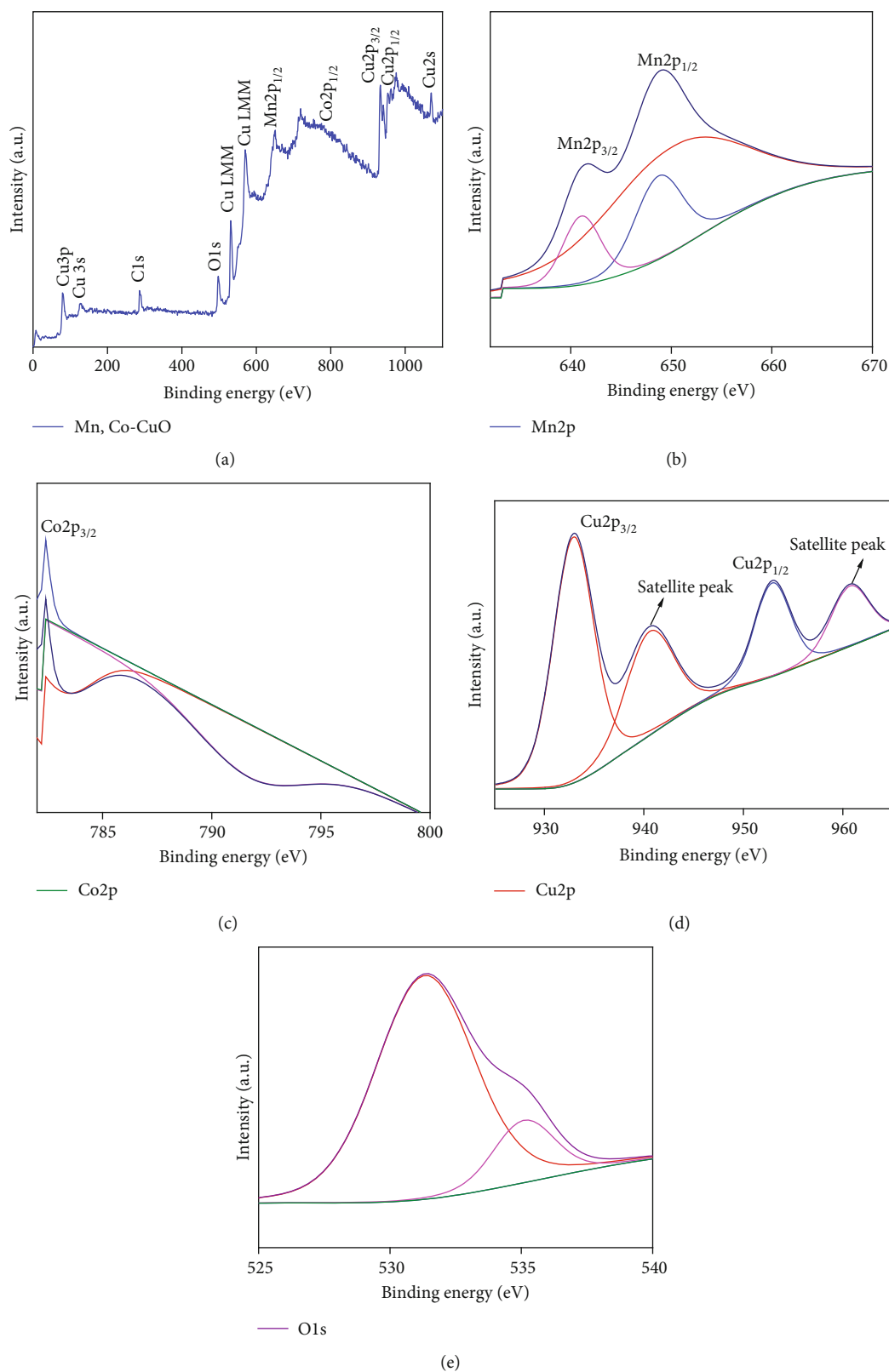
(a)

(b)

(c)

(d)

(e)

FIGURE 5: (a–e) XPS analysis of (Mn, Co) codoped CuO: (a) overall survey spectra of Mn, Co codoped CuO; (b–e) XPS core spectra of Mn, Co, Cu, and O.

at 932.71 eV and 952.67 eV indexed to $Cu2p_{3/2}$ and $Cu2p_{1/2}$, respectively, which are represented in Figure 5(d). In addition, 941.81 eV and 960.24 eV are attributed to $3d^9$ states of partially filled d block Cu^{2+} ions. Figure 5(e) shows the O1s spectra of the prepared Mn, Co codoped CuO electrode. The peaks at 531.10 eV O1s core level spectra are allocated to
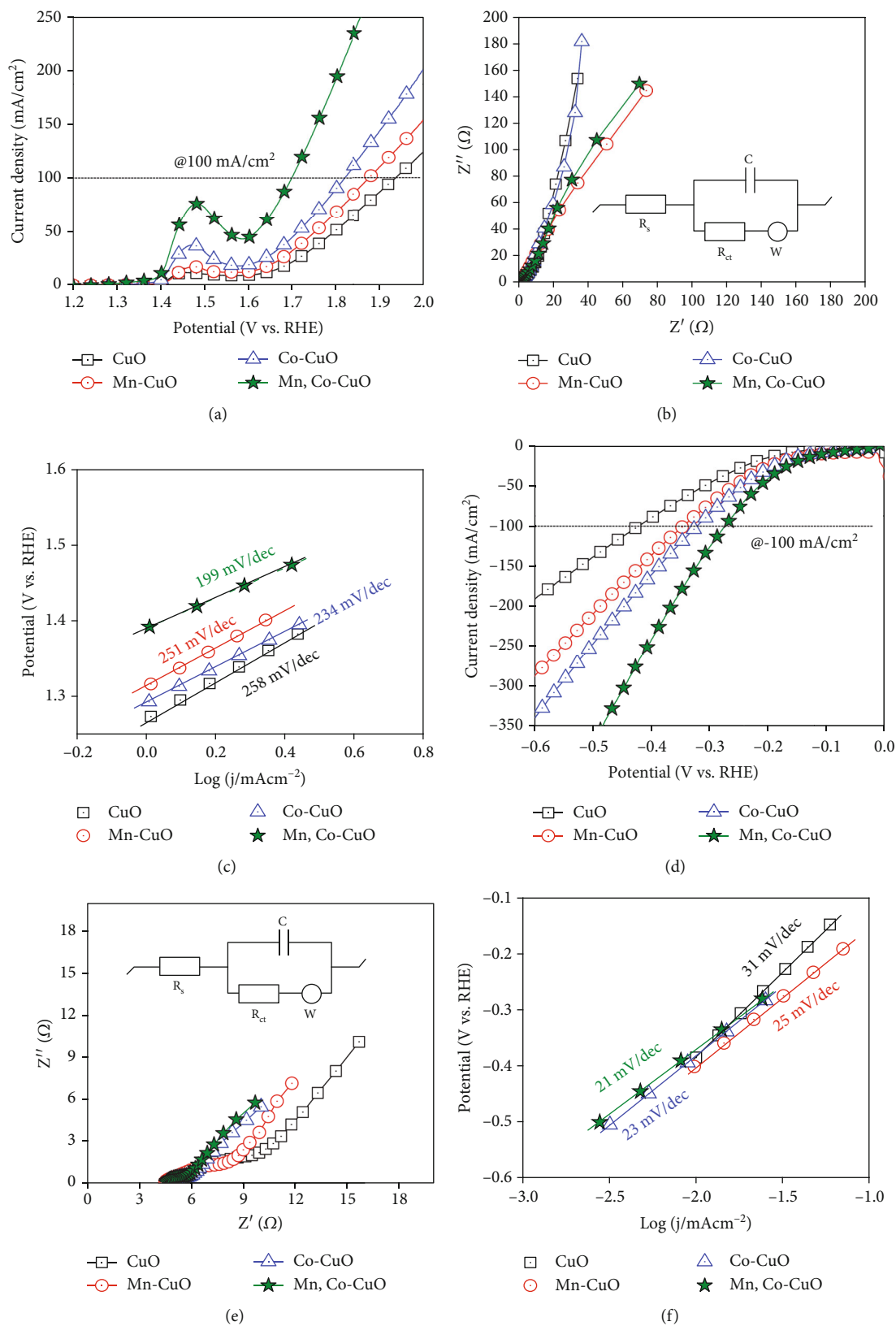
FIGURE 6: Electrocatalytic activity of Mn-, Co-, and codoped CuO nanoflakes in 1 M KOH: (a) OER-linear sweep voltammograms (LSVs); (b) Nyquist plot at 1.68 V vs. RHE potential; (c) OER-Tafel plot; (d) HER-linear sweep voltammograms (LSVs); (e) Nyquist plot at -0.2 V vs. RHE potential; (f) HER-Tafel plot.

TABLE 1: Comparison of overpotential with previous literature.

Electrode	Electrolyte	OER/HER	Overpotential	Ref.
CuO/Co_3O_4	1 M KOH	OER	450 mV @ 50 mA/cm^{-2}	[58]
$NiOOH@CuO-Cu_2O$	1 M KOH	OER	262 mV @ 20 mA/cm^{-2}	[59]
$Cu_2Se@CoSe$	1 M KOH	OER	320 mV @ 100 mA/cm^{-2}	[60]
Co-CuO nanoarray	1 M KOH	OER	330 mV @ 100 mA/cm^2	[61]
Cu@CoFe (LDH)	1 M KOH	HER&OER	171 mV for HER and 240 mV for OER @ 10 mA/cm^2	[62]
CuO@Ni/NiFe hydroxides	1 M KOH	HER&OER	230 mV for OER and 125 mV for HER @ 10 mA/cm^2	[63]
Mn, Co codoped CuO	1 M KOH	OER&HER	468 mV for OER and 271 mV for HER @ 100 mA/cm^{-2}	Present work

metal-oxygen bonding and adsorbed oxygen on CuO surface [54–56].

The fabricated electrodes were subjected to an electrochemical water-splitting application in the 1 M KOH alkaline electrolyte. Figure 6(a) demonstrates the linear sweep voltammogram (LSV) profile for OER activity (without ir correction). The lower overpotential and higher current density are achieved for Mn, Co codoped CuO nanoflakes. It requires the 468 mV overpotential to reach 100 mA/cm^2, where pure CuO (707 mV), Mn-doped CuO (648 mV), and Co-doped CuO (590 mV) require more overpotential than the codoped CuO electrode. The Nyquist plots at the OER potential of 1.68 V vs. RHE at 100 kHz to 100 MHz are presented in Figure 6(b), and the appropriate equivalent circuit was fitted as an inset. The solution resistance (R_s) of all four electrodes is similar. The charge transfer resistance (R_{ct}) of the Mn, Co codoped CuO electrode (3.6 Ω) is smaller than those of the pure CuO (7.1 Ω), Mn-doped (6.5 Ω), and Co-doped (6.0 Ω) CuO electrodes. Hence, faster electron transfer and active diffusion of the codoped electrode are further revealed from electrochemical impedance spectra (EIS) (matched with OER studies). The corresponding Tafel slope values for OER kinetics of all the four electrodes are illustrated in Figure 6(c). The lower Tafel slope value (199 mV/dec) of Mn, Co codoped CuO nanoflakes exposed their rapid OER kinetics compared to those of pure CuO (258 mV/dec), Mn-doped CuO (251 mV/dec), and Co-doped CuO (234 mV/dec) nanoflakes.

To examine the bifunctionality of the fabricated electrodes, the HER activity is also explored in 1 M KOH. Figure 6(d) shows the linear sweep voltammogram at the HER potential from 0 to -0.6 V vs. RHE (without ir correction). The Mn, Co codoped CuO revealed a lower HER overpotential (271 mV) to achieve 100 mA/cm^2 than other pure (426 mV), Mn-doped (347 mV), and Co-doped (328 mV) CuO electrodes. The EIS spectra at -0.2 V vs. RHE of all four electrodes from 100 kHz to 100 MHz are presented in Figure 6(e), and the appropriate circuits are shown as a fitted inset. Like OER kinetics, nearly similar R_s values for all the electrodes are observed. The lower R_{ct} of the Mn, Co codoped CuO (1.2 Ω) electrode represents the faster electron transfer than those of the pure (4.7 Ω), Mn-doped (3.7 Ω), and Co-doped CuO (1.5 Ω) electrodes. Thus, the Mn, Co codoped electrode also showed a faster electron transfer in the HER reaction, thus performing well as a bifunctional elec-

trode. The corresponding HER Tafel slopes (Figure 6(f)) further support the results of HER activity from the lower Tafel slope value afforded by the Mn, Co codoped CuO electrode (21 mV/dec) compared to others, which confirm the rapid reaction rate of the HER activity [57]. Thus, the bimetal (Mn, Co) codoped CuO nanoflake electrode exhibited the improved OER and HER kinetics compared to other undoped (CuO) and unary metal- (Mn- and Co-) doped CuO electrodes, which is due to the defect-enriched crystal structure (confirmed from XRD and Raman), optical property with respective emission regions and oxygen vacancies (confirmed from PL), and surface hydrophilicity (confirmed from FT-IR). In addition, the multiple valence states of Mn^{2+}/Mn^{3+} and Co^{2+}/Co^{3+} along with Cu^{2+} may facilitate a greater number of active centers to enrich the rapid reaction kinetics for overall water splitting. The bifunctional behavior of some previous literature reports are listed (Table 1). Overpotential is considered as one of the important parameters of electrochemical activity which has been compared with some other works in Table 1.

The cyclic voltammograms (CVs) of the fabricated electrodes at 1.30 to 1.40 V vs. RHE at 10 to 100 mV/s scan rates are shown in Figures 7(a)–7(d), to expose nonfaradaic capacitive behavior. From CVs, the electrochemical active surface area (ECSA) of electrodes is estimated and plotted in Figure 7(e), which strongly confirms that the Mn, Co codoped CuO electrode exhibited the higher double-layer capacitance (C_{dl}) as 27.5 mF/cm^2, and so possessed a higher ECSA. It is noticeably higher than those of the pure (13.8 mF/cm^2), Mn-doped (22.2 mF/cm^2), and Co-doped (24.8 mF/cm^2) CuO electrodes, possibly be due to the sharp-edge-exposed nanoflake morphology of Mn, Co codoped CuO with a smaller particle size, evidently increasing the faster electron transfer due to the presence of highly polarized edges to increase the ECSA and to enhance the overall water splitting [64].

The long-term chronoamperometry (CA) test over 16 h for both OER and HER actions of the Mn, Co codoped CuO at 1.67 and 0.186 V vs. RHE is shown in Figures 7(f) and 7(g). The image insets show the LSV graphs before and after stability. The OER CA test shows an excellent stability with almost no loss in the current density (Figure 7(g)), which confirms the sturdy nature of the electrode without any decay/corrosion of the surface reactivity. The LSV graph before and after the OER test (Figure 7(f)
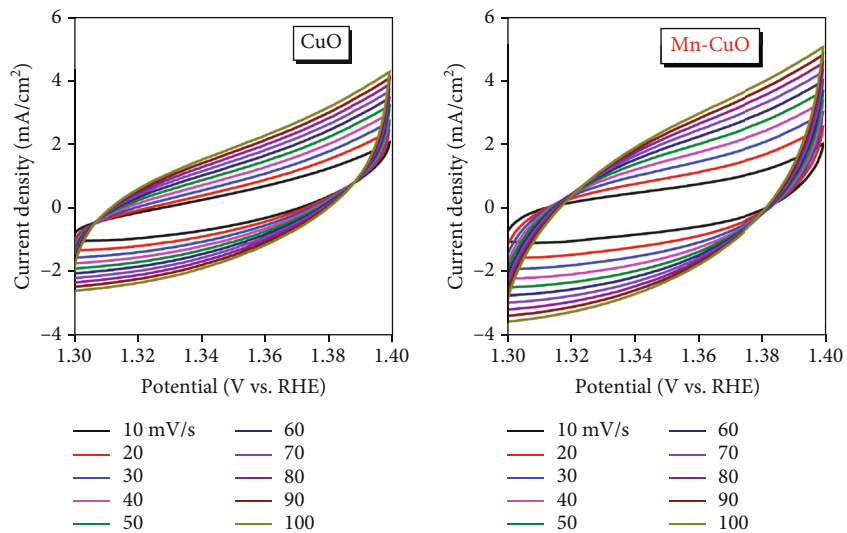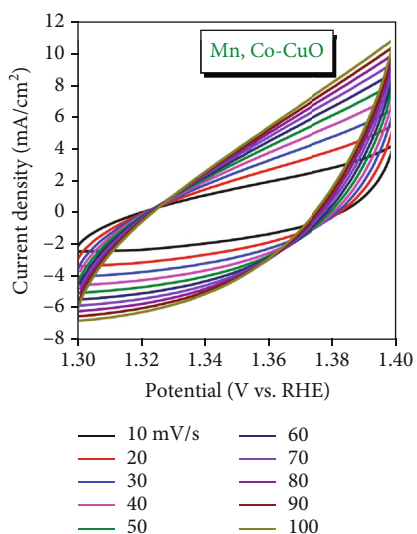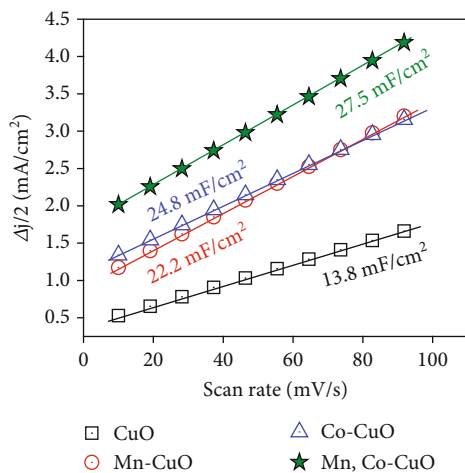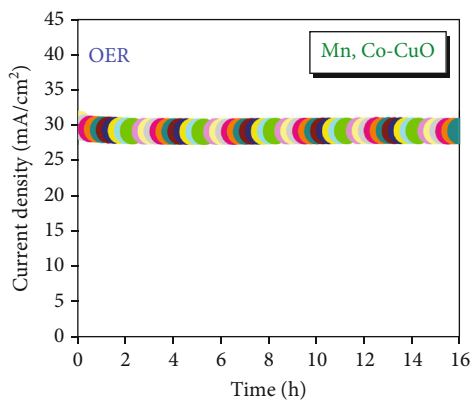
(a)

(b)
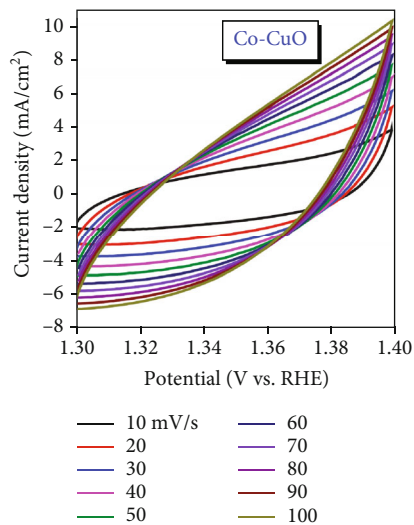
(c)

(d)
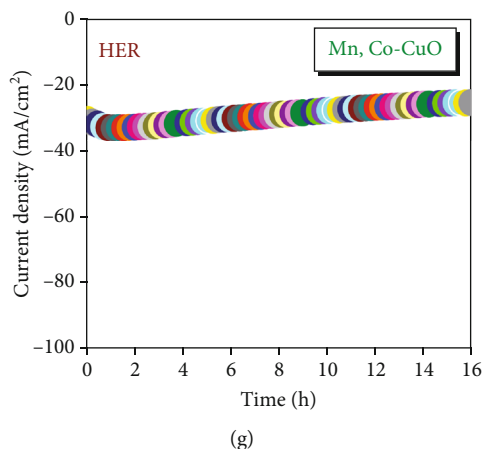

(e)

(f)

Figure 7: Continued.

FIGURE 7: Electrochemical active surface area (ECSA) and long-term stability in 1 M KOH: (a–d) cyclic voltammograms (CVs); (e) linear plots of ECSA; (f) OER-chronoamperometry (CA); (g) HER-chronoamperometry (CA). (Image insets are corresponding LSVs before and after CA test).

inset) supports the CA test that no overpotential change is observed after 16 h of continuous OER test in the alkaline electrolyte. The HER CA test shows 15% loss in the current density over time. Further, the LSV graph before and after the CA test (Figure 7(g), inset) shows the increase in overpotential observed after 16 h of continuous HER test, which might be because of the block of surface-active sites [65]. Hence, the Mn, Co codoped CuO electrode shows outstanding OER stability and good HER stability over 16 h of continuous water electrolysis. Moreover, the present study reports the exceptional performance of Mn, Co codoped CuO nanoflakes for achieving the higher 100 mA/cm^2 in both HER and OER activities compared to fabricated electrodes. Most studies focused only on the overpotential at low current densities like 10 or 20 mA/cm^2, which is insufficient for practical applications. This is because a typical water electrolyzer is operated at 300-400 mA/cm^2, and the cell voltage required is between 1.7 and 2.4 V [66]. Hence, it is possible to subject the Mn, Co codoped electrode to practical energy production systems without any issues in the near future.

The postcatalytic performance of the Mn, Co codoped CuO nanoflakes was investigated via scanning electron microscopy (SEM), to verify the morphological stability of the prepared sample which is shown in Figure S1(a–d). Figure S1(a, b) represents the post-SEM analysis of OER, and Figure S1(c, d) corresponds to the HER. It should be noted that the nanoflake morphology slightly decomposes into agglomerated tiny nanoparticles after the long cycling test over 20 h which possibly occurs due to the excessive bubble formation generated during the electrolysis reaction [67]. Moreover, compared with the pre- and post-SEM results in Figures 3(a)–3(d) and Figure S1(a–d), the attained nanoparticle morphology for OER and HER, that is, the structural stability, was moderately sustained after the long-term chronoamperometry activity. In order to confirm the structural and phase transformation of the Mn, Co codoped CuO electrode, the post-XRD study was done after electrochemical performances of OER and HER which is

presented in Figure S2(a). From Figure S2(b), the post-XRD pattern clearly revealed the existence of the main element Cu in the small intensity range at the lattice plane (110), (002), and (111) with respect to the 2θ degree values of 32.7°, 35.9°, and 38.7° which is well matched with the earlier reported JCPDS number #80-1268. Other than that, the high-intensity peaks denote the presence of the Ni element; this may happen due to the predominant influence of the Ni foam conductive substrate [68]. The chemical stability of the prepared electrode underwent the chronoamperometry test using the 1 M KOH electrolyte solution. The obtained results are presented in Figure S3(a, b) which reveal that the Mn, Co codoped CuO electrode withstands a long duration of up to 20 h with the least amount of loss corresponding to the postactivity of OER and HER. The chronoamperometry performance of OER at a low 10 mA/cm^2 (j_{10}) is initially reduced to 6.8 mA/cm^2 and is continuously sustained up to 20 h with 32% loss. Furthermore, at 10 mA/cm^2 (j_{10}), the HER electrode inclined slightly at 7.7 mA/cm^2 and remained stable for a prolonged duration of 20 h with 23% loss which is highly reliable for the bifunctional electrocatalytic performances. The electrocatalytic activities of both half-reactions attain stabilization after 5000 cycles. It denotes that the prepared Mn, Co codoped CuO electrode has exhibited great stability for a long duration after many CV cycles [69]. To further understand, the intrinsic active sites of the prepared sample were evaluated via turnover frequency (TOF) using the formula $(I \times N_A)/4Fn$ for OER and $(I \times N_A)/2Fn$ for HER, where I denotes the current in ampere (from LSV), N_A is the Avogadro number (6.022×10^{23}), 4 and 2 indicate the required number of electrons to form one oxygen and hydrogen molecule, F is the faradaic constant (96,485 C/mol), and n denotes the number of active sites. The overpotential value of $\eta_{10} = 468$ mV exhibits the TOF value of 0.36 s^{-1} and $\eta_{10} = 271$ mV attains the TOF value of 1.1 s^{-1} for OER and HER, respectively, which is clearly presented in Figure S4 and Table S1. These calculated values indicate that the Mn, Co codoped CuO achieves high TOF values compared to unary- (Mn- and Co-) doped CuO. Also, higher

TOF values assure the high intrinsic activity per catalytic site which is greatly beneficial for the outstanding electrocatalytic performance (detailed in supporting information) [70, 71].

4. Conclusions

In summary, Mn and Co codoping on CuO nanoflakes is produced via the coprecipitation method. Herein, we introduce the Mn, Co codoped CuO electrode as a competent bifunctional electrode for water splitting. Concentrated surface defects and oxygen vacancies and sharp-polarized-edge-centered nanoflakes of Mn, Co codoped CuO were reported for enhanced electrocatalytic activity. The abundant active sites (Mn^{2+}/Mn^{3+}, Co^{2+}/Co^{3+}, and Cu^{2+}) enhanced OER and HER activities at a high $100 \, mA/cm^2$ with less overpotential values such as $468 \, mV$ and $271 \, mV$, respectively, and the high double-layer capacitance value of $27.5 \, mF/cm^2$ has also been achieved to attain a large surface area for the proficient OER and HER performance. Robust OER and good HER stability performance over $16 \, h$ was achieved before the electrochemical analysis, and the $20 \, h$ stability performance after the electrochemical studies was taken and verified, exhibiting faster reaction kinetics and rapid charge transportation. The high intrinsic catalytic activity of Mn, Co codoped CuO nanoflakes was evaluated via the turnover frequency with the values of $0.34 \, s^{-1}$ and $1.1 \, s^{-1}$ for OER and HER, respectively. The excellent stability of the prepared electrode for prolonged duration in OER and HER at an elevated current density which is favorable and is suggested for a large-scale marketable application and a high surface area with high current density proves that the Mn, Co codoped CuO nanostructure is able to act as a successful anode and cathode material to avoid energy loss during the energy conversion progress. In the future, we will plan to incorporate the carbon-based composites like graphene, graphitic carbon nitride, and carbon nanotubes to develop the catalytic activity and durability which has also become one of the sustainable alternatives for the growing energy demand. Hence, achieving high current density ($100 \, mA/cm^2$) with low driving force and striking stability for overall water splitting using an earth-abundant electrocatalyst was reported in this work, which would serve greater contribution to the real-time pragmatism in electrocatalytic water splitting. Hopefully, it may become a problem-solving electrocatalyst in the field of energy shortage environmental problems.

Data Availability

Data are available on request.

Conflicts of Interest

The authors hereby declare that there is no conflict of interest.

Acknowledgments

Supplementary Materials

Postcatalytic performance of Mn, Co codoped CuO nanoflakes investigated by scanning electron microscopy (SEM). Figure S1: post-SEM analysis of Mn, Co codoped CuO after the OER and HER electrochemical studies. Figure S2: post-XRD analysis of Mn, Co codoped CuO nanoflakes. Figure S3: chronoamperometry test for prepared electrode after the OER and HER electrochemical studies. Figure S4: active site analysis from CV curves (inset: bar diagram). Table S1: assessed TOF values for Mn, Co codoped CuO nanoflakes. *(Supplementary Materials)*

References

[1] K. Chhetri, A. Muthurasu, B. Dahal et al., "Engineering the abundant heterointerfaces of integrated bimetallic sulfide-coupled 2D MOF-derived mesoporous CoS_2 nanoarray hybrids for electrocatalytic water splitting," *Materials Today Nano*, vol. 17, article 100146, 2022.

[2] S. Li, E. Li, X. An, X. Hao, Z. Jiang, and G. Guan, "Transition metal-based catalysts for electrochemical water splitting at high current density: current status and perspectives," *Nanoscale*, vol. 13, no. 30, pp. 12788–12817, 2021.

[3] Z. Chen, W. Wei, and B. J. Ni, "Cost-effective catalysts for renewable hydrogen production via electrochemical water splitting: recent advances," *Current Opinion in Green and Sustainable Chemistry*, vol. 27, article 100398, 2021.

[4] S. Jiao, X. Fu, S. Wang, and Y. Zhao, "Perfecting electrocatalysts via imperfections: towards the large-scale deployment of water electrolysis technology," *Energy & Environmental Science*, vol. 14, no. 4, pp. 1722–1770, 2021.

[5] X. Hu, X. Tian, Y.-W. Lin, and Z. Wang, "Nickel foam and stainless steel mesh as electrocatalysts for hydrogen evolution reaction, oxygen evolution reaction and overall water splitting in alkaline media," *RSC Advances*, vol. 9, no. 54, pp. 31563–31571, 2019.

[6] X. Han, N. Suo, C. Chen et al., "Graphene oxide guiding the constructing of nickel-iron layered double hydroxides arrays as a desirable bifunctional electrocatalyst for HER and OER," *International Journal of Hydrogen Energy*, vol. 44, no. 57, pp. 29876–29888, 2019.

[7] D. D. Qin, Y. Tang, G. Ma et al., "Molecular metal nanoclusters for ORR, HER and OER: achievements, opportunities, and challenges," *International Journal of Hydrogen Energy*, vol. 46, no. 51, pp. 25771–25781, 2021.

[8] E. Kemppainen, A. Bodin, B. Sebok et al., "Scalability and feasibility of photoelectrochemical H_2 evolution: the ultimate limit of Pt nanoparticle as an HER catalyst," *Energy & Environmental Science*, vol. 8, no. 10, pp. 2991–2999, 2015.

[9] S. Anantharaj, P. E. Karthik, B. Subramanian, and S. Kundu, "Pt nanoparticle anchored molecular self-assemblies of DNA: an extremely stable and efficient HER electrocatalyst with ultralow Pt content," *ACS Catalysis*, vol. 6, no. 7, pp. 4660–4672, 2016.

[10] K. S. Exner, J. Anton, T. Jacob, and H. Over, "Ligand effects and their impact on electrocatalytic processes exemplified with

the oxygen evolution reaction (OER) on RuO_2 (110)," *Chem-ElectroChem*, vol. 2, no. 5, pp. 707–713, 2015.

[11] Y. Lee, J. Suntivich, K. J. May, E. E. Perry, and Y. Shao-Horn, "Synthesis and activities of rutile IrO_2 and RuO_2 nanoparticles for oxygen evolution in acid and alkaline solutions," *The Journal of Physical Chemistry Letters*, vol. 3, no. 3, pp. 399–404, 2012.

[12] B. K. Hong, S. H. Kim, and C. M. Kim, "Powering the future through hydrogen and polymer electrolyte membrane fuel cells," *Johnson Matthey Technology Review*, vol. 64, p. 236, 2020.

[13] P. Poizot and F. Dolhem, "Clean energy new deal for a sustainable world: from non-CO_2 generating energy sources to greener electrochemical storage devices," *Energy & Environmental Science*, vol. 4, no. 6, pp. 2003–2019, 2011.

[14] S. Lv, J. Li, B. Zhang, Y. Shi, X. Liu, and T. Wang, "In-situ growth of hierarchical $CuO@Cu_3P$ heterostructures with transferable active centers on copper foam substrates as bifunctional electrocatalysts for overall water splitting in alkaline media," *International Journal of Hydrogen Energy*, vol. 47, no. 16, pp. 9593–9605, 2022.

[15] L. Yin, X. Du, C. Di, M. Wang, K. Su, and Z. Li, "In-situ transformation obtained defect-rich porous hollow $CuO@CoZn$-LDH nanoarrays as self-supported electrode for highly efficient overall water splitting," *Chemical Engineering Journal*, vol. 414, article 128809, 2021.

[16] A. Maiti and S. K. Srivastava, "Ru-doped CuO/MoS_2 nano-structures as bifunctional water-splitting electrocatalysts in alkaline media," *ACS Applied Nano Materials*, vol. 4, no. 8, pp. 7675–7685, 2021.

[17] D. Ghosh and D. Pradhan, "Effect of Cooperative Redox Property and Oxygen Vacancies on Bifunctional OER and HER Activities of Solvothermally Synthesized CeO2/CuO Composites," *Langmuir*, vol. 39, no. 9, pp. 3358–3370, 2023.

[18] W. Jia, E. Reitz, P. Shimpi, E. G. Rodriguez, P. X. Gao, and Y. Lei, "Spherical CuO synthesized by a simple hydrothermal reaction: concentration-dependent size and its electrocatalytic application," *Materials Research Bulletin*, vol. 44, no. 8, pp. 1681–1686, 2009.

[19] D. Chi, H. Yang, Y. Du et al., "Morphology-controlled CuO nanoparticles for electroreduction of CO_2 to ethanol," *RSC Advances*, vol. 4, no. 70, pp. 37329–37332, 2014.

[20] T. Soejima, K. Takada, and S. Ito, "Alkaline vapor oxidation synthesis and electrocatalytic activity toward glucose oxidation of CuO/ZnO composite nanoarrays," *Applied Surface Science*, vol. 277, pp. 192–200, 2013.

[21] A. Tahira, Z. H. Ibupoto, M. Willander, and O. Nur, "Advanced Co_3O_4-CuO nano-composite based electrocatalyst for efficient hydrogen evolution reaction in alkaline media," *International Journal of Hydrogen Energy*, vol. 44, no. 48, pp. 26148–26157, 2019.

[22] J. Jiang, F. Sun, S. Zhou et al., "Atomic-level insight into super-efficient electrocatalytic oxygen evolution on iron and vanadium co-doped nickel (oxy)hydroxide," *Nature Communications*, vol. 9, no. 1, article 2885, 2018.

[23] S. Chen, T. Liu, S. O. Olanrele et al., "Boosting electrocatalytic activity for CO_2 reduction on nitrogen-doped carbon catalysts by co-doping with phosphorus," *Journal of Energy Chemistry*, vol. 54, pp. 143–150, 2021.

[24] D. M. Morales, M. A. Kazakova, S. Dieckhöfer et al., "Trimetallic Mn-Fe-Ni oxide nanoparticles supported on multi-walled carbon nanotubes as high-performance bifunctional ORR/OER electrocatalyst in alkaline media," *Advanced Functional Materials*, vol. 30, no. 6, article 1905992, 2020.

[25] Q. Qin, L. Chen, T. Wei, Y. Wang, and X. Liu, "Ni/NiM_2O_4 (M = Mn or Fe) supported on N-doped carbon nanotubes as trifunctional electrocatalysts for ORR, OER and HER," *Catalysis Science & Technology*, vol. 9, no. 7, pp. 1595–1601, 2019.

[26] C. C. Yang, S. F. Zai, Y. T. Zhou, L. du, and Q. Jiang, "Fe_3C-Co nanoparticles encapsulated in a hierarchical structure of N-doped carbon as a multifunctional electrocatalyst for ORR, OER, and HER," *Advanced Functional Materials*, vol. 29, no. 27, article 1901949, 2019.

[27] X. Yuan, H. Ge, X. Wang et al., "Controlled phase evolution from Co nanochains to CoO nanocubes and their application as OER catalysts," *ACS Energy Letters*, vol. 2, no. 5, pp. 1208–1213, 2017.

[28] D. Ding, K. Shen, X. Chen et al., "Multi-level architecture optimization of MOF-templated Co-based nanoparticles embedded in hollow N-doped carbon polyhedra for efficient OER and ORR," *ACS Catalysis*, vol. 8, no. 9, pp. 7879–7888, 2018.

[29] Z. Niu, C. Qiu, J. Jiang, and L. Ai, "Hierarchical CoP-FeP branched heterostructures for highly efficient electrocatalytic water splitting," *ACS Sustainable Chemistry & Engineering*, vol. 7, no. 2, pp. 2335–2342, 2019.

[30] P. Zhang, X. F. Lu, J. Nai, S. Q. Zang, and X. W. (. D.). Lou, "Construction of hierarchical Co–Fe oxyphosphide microtubes for electrocatalytic overall water splitting," *Advanced Science*, vol. 6, no. 17, article 1900576, 2019.

[31] B. P. Singh, M. Chaudhary, A. Kumar et al., "Effect of Co and Mn doping on the morphological, optical and magnetic properties of CuO nanostructures," *Solid State Sciences*, vol. 106, article 106296, 2020.

[32] A. A. Manoharan, R. Chandramohan, R. D. Prabu et al., "Facile synthesis and characterization of undoped, Mn doped and Nd co-doped CuO nanoparticles for optoelectronic and magnetic applications," *Journal of Molecular Structure*, vol. 1171, pp. 388–395, 2018.

[33] B. J. Rani, M. Ravina, G. Ravi, S. Ravichandran, V. Ganesh, and R. Yuvakkumar, "Synthesis and characterization of hausmannite (Mn_3O_4) nanostructures," *Surfaces and Interfaces*, vol. 11, pp. 28–36, 2018.

[34] B. Jansi Rani, G. Ravi, R. Yuvakkumar et al., "Bi_2WO_6 and $FeWO_4$ nanocatalysts for the electrochemical water oxidation process," *ACS Omega*, vol. 4, no. 3, pp. 5241–5253, 2019.

[35] B. J. Rani, G. Ravi, R. Yuvakkumar, and S. I. Hong, "Novel $SmMn_2O_5$ hollow long nano-cuboids for electrochemical supercapacitor and water splitting applications," *Vacuum*, vol. 166, pp. 279–285, 2019.

[36] W. Zhang, S. Ding, Z. Yang et al., "Growth of novel nanostructured copper oxide (CuO) films on copper foil," *Journal of Crystal Growth*, vol. 291, no. 2, pp. 479–484, 2006.

[37] D. J. Kim, "Lattice parameters, ionic conductivities, and solubility limits in fluorite-structure MO_2 oxide [M = Hf^{4+}, Zr^{4+}, Ce^{4+}, Th^{4+}, U^{4+}] solid solutions," *Journal of the American Ceramic Society*, vol. 72, no. 8, pp. 1415–1421, 1989.

[38] B. J. Rani, M. Ravina, B. Saravanakumar et al., "Ferrimagnetism in cobalt ferrite ($CoFe_2O_4$) nanoparticles," *Nano-Structures & Nano-Objects*, vol. 14, pp. 84–91, 2018.

[39] P. G. Etchegoin and E. C. Le Ru, "Resolving single molecules in surface-enhanced Raman scattering within the inhomogeneous

broadening of Raman peaks," *Analytical Chemistry*, vol. 82, no. 7, pp. 2888–2892, 2010.

[40] T. Yu, X. Zhao, Z. X. Shen, Y. H. Wu, and W. H. Su, "Investigation of individual CuO nanorods by polarized micro-Raman scattering," *Journal of Crystal Growth*, vol. 268, no. 3-4, pp. 590–595, 2004.

[41] J. F. Xu, W. Ji, Z. X. Shen et al., "Raman spectra of CuO nanocrystals," *Journal of Raman Spectroscopy*, vol. 30, no. 5, pp. 413–415, 1999.

[42] B. J. Rani, G. Ravi, R. Yuvakkumar, Z. M. Hasan, S. Ravichandran, and S. I. Hong, "Binder free, robust and scalable CuO@GCE modified electrodes for efficient electrochemical water oxidation," *Materials Chemistry and Physics*, vol. 239, article 122321, 2020.

[43] B. J. Rani, G. Ravi, R. Yuvakkumar, S. Ravichandran, F. Ameen, and A. Al-Sabri, "Efficient, highly stable Zn-doped NiO nanocluster electrocatalysts for electrochemical water splitting applications," *Journal of Sol-Gel Science and Technology*, vol. 89, no. 2, pp. 500–510, 2019.

[44] A. Azam, A. S. Ahmed, M. Oves, M. S. Khan, and A. Memic, "Size-dependent antimicrobial properties of CuO nanoparticles against gram-positive and -negative bacterial strains," *International Journal of Nanomedicine*, vol. 7, pp. 3527–3535, 2012.

[45] B. J. Rani, S. P. Raj, B. Saravanakumar et al., "Controlled synthesis and electrochemical properties of Ag-doped Co_3O_4 nanorods," *International Journal of Hydrogen Energy*, vol. 42, no. 50, pp. 29666–29671, 2017.

[46] S. Chen, J. Duan, M. Jaroniec, and S. Z. Qiao, "Nitrogen and oxygen dual-doped carbon hydrogel film as a substrate-free electrode for highly efficient oxygen evolution reaction," *Advanced Materials*, vol. 26, no. 18, pp. 2925–2930, 2014.

[47] A. S. Mary, C. Murugan, and A. Pandikumar, "Uplifting the charge carrier separation and migration in Co-doped CuBi2O4/TiO2pn heterojunction photocathode for enhanced photoelectrocatalytic water splitting," *Journal of Colloid and Interface Science*, vol. 608, pp. 2482–2492, 2022.

[48] M. Bilal, M. Ikram, T. Shujah et al., "Chitosan-grafted polyacrylic acid-doped copper oxide nanoflakes used as a potential dye degrader and antibacterial agent: in silico molecular docking analysis," *ACS Omega*, vol. 7, no. 45, pp. 41614–41626, 2022.

[49] S. Kulkarni, S. Kummara, G. Gorthala, and R. Ghosh, "CuO nanoflake-based sensors for detecting linalool, hexanal, and methyl salicylate," *ACS Agricultural Science & Technology*, vol. 2, no. 6, pp. 1285–1291, 2022.

[50] S. Rajasekar, V. Tiwari, U. Srivastva, and S. Holdcroft, "Effectiveness of CuO nanoparticle-based p–n bulk-heterojunction electrodes for photoelectrochemical hydrogen generation," *ACS Applied Energy Materials*, vol. 3, no. 9, pp. 8988–9001, 2020.

[51] A. ur Rehman, M. Aadil, S. Zulfiqar et al., "Fabrication of binary metal doped CuO nanocatalyst and their application for the industrial effluents treatment," *Ceramics International*, vol. 47, no. 5, pp. 5929–5937, 2021.

[52] X. Guo, H. Ge, Z. Sun et al., "Chemical coupling of manganese–cobalt oxide and oxidized multi-walled carbon nanotubes for enhanced lithium storage," *Journal of Colloid and Interface Science*, vol. 618, pp. 322–332, 2022.

[53] M. U. Tahir, H. Arshad, H. Zhang et al., "Room temperature and aqueous synthesis of bimetallic ZIF derived CoNi layered double hydroxides and their applications in asymmetric supercapacitors," *Journal of Colloid and Interface Science*, vol. 579, pp. 195–204, 2020.

[54] M. R. Kandel, U. N. Pan, P. P. Dhakal et al., "Unique heterointerface engineering of Ni_2P–MnP nanosheets coupled Co_2P nanoflowers as hierarchical dual-functional electrocatalyst for highly proficient overall water-splitting," *Applied Catalysis B: Environmental*, vol. 331, article 122680, 2023.

[55] A. K. Mishra and D. Pradhan, "Hierarchical urchin-like cobalt-doped CuO for enhanced electrocatalytic oxygen evolution reaction," *ACS Applied Energy Materials*, vol. 4, no. 9, pp. 9412–9419, 2021.

[56] M. R. Kandel, U. N. Pan, D. R. Paudel, P. P. Dhakal, N. H. Kim, and J. H. Lee, "Hybridized bimetallic phosphides of Ni–Mo, Co–Mo, and Co–Ni in a single ultrathin-3D-nanosheets for efficient HER and OER in alkaline media," *Composites Part B: Engineering*, vol. 239, article 109992, 2022.

[57] J. D. Rodney, S. Deepapriya, M. C. Robinson et al., "Dysprosium doped copper oxide ($Cu_{1-x}Dy_xO$) nanoparticles enabled bifunctional electrode for overall water splitting," *International Journal of Hydrogen Energy*, vol. 46, no. 54, pp. 27585–27596, 2021.

[58] S. Y. Zhang, H. L. Zhu, and Y. Q. Zheng, "Surface modification of CuO nanoflake with Co_3O_4 nanowire for oxygen evolution reaction and electrocatalytic reduction of CO_2 in water to syngas," *Electrochimica Acta*, vol. 299, pp. 281–288, 2019.

[59] Y. Li, G. Li, J. Xu, and L. Jia, "Novel CuO–Cu_2O redox-induced self-assembly of hierarchical $NiOOH@CuO$–$Cu_2O/Co(OH)_2$ nanocomposite for efficient oxygen evolution reaction," *Sustainable Energy & Fuels*, vol. 4, no. 2, pp. 869–877, 2020.

[60] X. Wang, Y. Zhou, Y. Tuo et al., "Synthesis and identifying the active site of $Cu_2Se@CoSe$ nano-composite for enhanced electrocatalytic oxygen evolution," *Electrochimica Acta*, vol. 320, p. 134589, 2019.

[61] X. Xiong, C. You, Z. Liu, A. M. Asiri, and X. Sun, "Co-doped CuO nanoarray: an efficient oxygen evolution reaction electrocatalyst with enhanced activity," *ACS Sustainable Chemistry & Engineering*, vol. 6, no. 3, pp. 2883–2887, 2018.

[62] L. Yu, H. Zhou, J. Sun et al., "Hierarchical Cu@CoFe layered double hydroxide core-shell nanoarchitectures as bifunctional electrocatalysts for efficient overall water splitting," *Nano Energy*, vol. 41, pp. 327–336, 2017.

[63] Y. Liu, Z. Jin, X. Tian, X. Li, Q. Zhao, and D. Xiao, "Core-shell copper oxide @ nickel/nickel–iron hydroxides nanoarrays enabled efficient bifunctional electrode for overall water splitting," *Electrochimica Acta*, vol. 318, pp. 695–702, 2019.

[64] X. Zhong, S. Liang, T. Yang et al., "Sn dopants with synergistic oxygen vacancies boost CO2 electroreduction on CuO nanosheets to CO at low overpotential," *ACS Nano*, vol. 16, no. 11, pp. 19210–19219, 2022.

[65] J. Zhang, Z. Huang, Y. du, X. Wu, H. Shen, and G. Jing, "Alkali-poisoning-resistant $Fe_2O_3/MoO_3/TiO_2$ Catalyst for the selective reduction of NO by NH_3: the role of the MoO_3 Safety buffer in protecting surface active sites," *Environmental Science & Technology*, vol. 54, no. 1, pp. 595–603, 2020.

[66] A. Buttler and H. Spliethoff, "Current status of water electrolysis for energy storage, grid balancing and sector coupling via power-to-gas and power-to-liquids: a review," *Renewable and Sustainable Energy Reviews*, vol. 82, pp. 2440–2454, 2018.

[67] P. C. Rath, J. Patra, D. Saikia et al., "Comparative study on the morphology-dependent performance of various CuO nanostructures as anode materials for sodium-ion batteries," *ACS*

Sustainable Chemistry & Engineering, vol. 6, no. 8, pp. 10876–10885, 2018.

[68] P. K. Raul, S. Senapati, A. K. Sahoo et al., "CuO nanorods: a potential and efficient adsorbent in water purification," *RSC Advances*, vol. 4, no. 76, pp. 40580–40587, 2014.

[69] W. Zheng, X. Ma, H. Sun et al., "Fe–Ni–Co trimetallic oxide hierarchical nanospheres as high-performance bifunctional electrocatalysts for water electrolysis," *New Journal of Chemistry*, vol. 46, no. 27, pp. 13296–13302, 2022.

[70] Y. Yan, B. Xia, X. Ge, Z. Liu, J. Y. Wang, and X. Wang, "Ultra-thin MoS_2 nanoplates with rich active sites as highly efficient catalyst for hydrogen evolution," *ACS Applied Materials & Interfaces*, vol. 5, no. 24, pp. 12794–12798, 2013.

[71] N. U. A. Babar and K. S. Joya, "Spray-coated thin-film Ni-oxide nanoflakes as single electrocatalysts for oxygen evolution and hydrogen generation from water splitting," *ACS Omega*, vol. 5, no. 19, pp. 10641–10650, 2020.